# Photo-active and Optical Properties of Bismuth Ferrite ($BiFeO_3$): An Experimental and Theoretical Study

Kevin A. McDonnell[1,2], Nitin Wadnerkar[3,*], Niall J. English[2,3,*], Mahfujur Rahman[2] and Denis Dowling[1,2,*]

[1]*School of Mechanical and Materials Engineering, University College Dublin, Belfield, Dublin 4, Ireland*

[2]*The SEC Strategic Research Cluster and the Centre for Synthesis and Chemical Biology, School of Chemical and Bioprocess Engineering, University College Dublin, Belfield, Dublin 4, Ireland*

[3]*The SFI Strategic Research Cluster in Solar Energy Conversion, School of Chemical and Bioprocess Engineering, University College Dublin, Belfield, Dublin 4, Ireland*

An experimental and a hybrid density functional theory study of the photo-active and optical properties of bismuth ferrite are presented. Phase-pure photo-catalytically active BFO was prepared experimentally with a 28% degradation of methyl orange observed over a 7-hour period. Direct and indirect band gaps were measured to be 2.10 and 1.92 eV, respectively. BFO was also studied computationally with the use of hybrid density functional theory, quite suitable for such a multiferroelectric material. This led to excellent, semi-quantitative agreement between hybrid DFT and experimental approaches for absorption coefficients.

Keywords: Bismuth Ferrite, Absorption, Density Functional Theory, Optical Properties

*Corresponding Author
Tel: + 353-1-716-1747 (DD), -1646 (NE); Fax: + 353-1-283-0534 (DD), -1177 (NE)
E-mail: niall.english@ucd.ie (NE), wadnerkar_nitin@yahoo.com (NW), denis.dowling@ucd.ie (DD)

## 1. Introduction

Bismuth ferrite (BFO, $BiFeO_3$) has a rhombohedrally distorted perovskite structure [1], and since its discovery in the 1960's has attracted much attention due to its unique ferromagnetic properties [2] and extensive list of applications from memory storage and spintronics to sensors. Recent studies have also indicated that BFO, due to its band gap of ~2 eV and good chemical stability makes a very good visible light responsive photo-catalytic material [3]. As a result of ever-increasing interest in this material, numerous preparation methods have been explored for the production of BFO, including wet chemical and mechanical methods, such as sol gel [4], co-precipitation [5], rapid liquid sintering [6] and mechanical activation[7].

Li *et al* [8] have used a wet chemical technique to produce BFO crystals for a range of sizes and morphologies. It was concluded that the variation in particle size and morphology had a substantial effect on the band gap. The variation in particle size between the micro- and nano-scale sees the band gap change from 1.80 to 2.19 eV, with photo-catalytic decomposition of congo red varying from 15 to 95%. Srivastav *et al* [9] have shown through propylene glycol-based synthesis that the produced nano-particles exhibited weak ferromagnetic properties at room temperature with a band gap of 2.1 eV.

With all methods of synthesis, there is a difficulty in the preparation of phase-pure BFO due to the narrow temperature range of phase stabilisation. Mechanical methods of preparation are highly susceptible to the creation of such unwanted phases. However, the utilisation of a leaching step in nitric acid essentially obviates these and makes this facile method of powder preparation attractive. This study utilises a conventional solid-state reaction route for the synthesis of BFO outlined by Kumar *et al.* [10]. In this process, stoichiometric amounts of metal oxide powders of bismuth and iron oxide are mixed thoroughly and calcined at high temperatures.

In recent years, the accurate characterisation of the electronic structure of BFO by Density Functional theory (DFT) remains elusive, although there have been a number of studies devoted to this [11-14]. The band gaps of transition metal oxides are underestimated routinely by the generalised gradient approximation (GGA) of DFT due to the less accurate description of strong Coulomb and exchange interactions between electrons in the same *d*-shell. Neaton *et al.* [13] investigated the spontaneous polarization in BFO using LSDA+U techniques and obtained a band gap of approximately 1.9 eV. Recently, Clark and Robertson [12] estimated a band gap of 2.8 eV, suggesting underestimation due to LSDA. Bilc *et al.* [11] estimated a band gap of 3.0-3.6 eV using B1-WC and B3LYP functional [14]. On the other hand, there have been several estimations of experimental band gap values which vary from 2.1 to 2.8 eV [15-21]. In addition, while comparing the results, it is somewhat problematic to compare the theoretical band gap from bulk DFT calculations with experiments using thin films: optical band gap values may differ due to thickness of thin films. In support of this, the computed DFT band gap versus thickness of thin film has been discussed by Micha *et al.* [22]. In recent studies, Goffinet *et al.* [23] and Pozun *et al.* [24] have estimated band gap values closer to experimental data using hybrid DFT, and these can be considered to be valuable alternatives to LDA, GGA and DFT+U; however, the important matter of optical properties have not been fully described, given BFO's photo-catalytic potential. Unlike the DFT+U approach, hybrid-DFT does not contain *d*-electron-specific empirical parameters. But this approach may break the spin and orbital symmetry of correlated metals or insulators. Motivated by these studies, we apply in this work a hybrid functional method which mixes a portion of exact Fock exchange with the DFT functional. This use of hybrid functionals gives very good results in comparison to our experiments, and suggests a possible underlying explanation for the optical properties of BFO. Here, we have combined XRD, UV-vis spectroscopy and photo-degradation studies with state-of-the-art hybrid-DFT calculations to probe the

crystalline and electronic band structure along with optical properties, using experimental methods in tandem with the HSE06-PBEsol functional (with 10% exact exchange) to give essentially correct geometry. Although not tested for other multiferroelectric materials the reliability of band gaps using this functional has been tested and tuned using a different bismuth oxide material ($BiVO_4$) with the same amount of exact exchange in our recent work [25]. This method is easier to apply and cheaper than the standard GW method which is essentially running a coupled cluster correction.

## 2. Materials and Methods

### 2.1 Experimental

Bismuth ferrite was synthesised by a solid-state reaction outlined by Kumar *et al.* [10]. Stoichiometric measurements (1:1) of Bismuth (III) Oxide ($Bi_2O_3$) (99.999% pure, Sigma Aldrich) and Iron (III) Oxide ($Fe_2O_3$) nano-powder (Sigma Aldrich) were measured using a high-precision balance; 4.6596g of $Bi_2O_3$ and 1.5969g of $Fe_2O_3$. The powders were mixed thoroughly with a mortar and pestle with a small amount of high-purity isopropanol. The powder was pre-calcined at 650°C for 1 hour before being reground and heated at 810°C for a further hour. After thermal treatment, further grinding was conducted before leaching the powder in 20 ml of 1.0 M solution of nitric acid for 3 hours to remove unwanted impurities. The leached solution was passed through filter paper and the powder remnants washed with de-ionised water and isopropanol to remove any remaining acid. The powder was further dried at 100 °C for 30 minutes.

The degree of crystallinity and the phase composition of the coatings were examined by a Siemens D500 X-ray diffractometer (XRD) operating at 40 kV and 30 mA with Cu Kα radiation at a wavelength of 0.1542 nm. The scan was conducted in the 2θ-mode and spanned across a range of 20 to 80° with a step resolution of 0.02°.

Particle-size distribution analysis of the powder was conducted using a Sympatec HELOS laser diffraction based Particle-Size Analyser (PSA). A small quantity of BFO was made into a paste with a dispersing agent before adding to purified deionised water. The mixture was stirred with a magnetic stirrer to agitate the particulates and disperse them evenly throughout the liquid.

Light absorption was measured using an Analytik Jena Specord 210 UV-vis spectrometer configured in reflectance mode, using an integrating-sphere attachment. The scan was conducted over a spectral range of 290 to 800 nm. To examine the morphological structure of the synthesised powder, a small amount was placed on an adhesive conductive pad and examined directly in a Hitachi SEM.

A study into the photo-degradation of methyl orange was conducted to investigate if the synthesised $BiFeO_3$ exhibited photo-catalytic behaviour. A Suntest CPS + system equipped with a 1500 W Xenon lamp and solar filter was used for the study. A stock solution of $x10^{-4}$M methyl orange was prepared, as this was deemed to be the optimum concentration for degradation under solar illumination [26]. 40 ml solutions of methyl orange, bismuth ferrite and titanium dioxide ($TiO_2$) of 30 mM concentration were prepared. Each solution was bubbled with oxygen for 15 minutes before being placed into the Suntest machine, where they were agitated in the dark with a magnetic stirrer for 30 minutes. A 4 ml aliquot was taken, passed through a syringe filter, placed in a small brown glass vial and then stored in the dark to prevent further degradation. The xenon lamp was switched on and 4 ml aliquots were taken at 60-minute intervals for 7 hours. The absorption spectrum of the filtered liquids was measured using a UV-Vis spectrometer in transmission mode.

## 2.2 Theoretical

The calculations reported herein were performed using three-dimensional periodic spin-polarised density functional theory (DFT) calculations within the generalized gradient approximation (GGA) using the Heyd-Scuseria-Ernzerhof (HSE06) hybrid functional [27-29], as implemented in the Vienna *ab initio* Simulation Package (VASP) code (v5.2.11) [30, 31] in conjunction with projector-augmented wave (PAW) pseudo-potentials. The exchange-correlation potential was divided into short-and long-range parts, and Hartree-Fock (HF) exchange-correlation was mixed with Perdew-Burke-Ernzerhof (PBEsol) exchange-correlation, as adjusted for solids [27], in the short-range part. PBEsol has been used due to its superior geometry prediction vis-à-vis PBE exchange-correlation in solids [32, 33] leading to more accurate Born-Oppenheimer forces acting on the electronic wave-functions, and providing the best feasible estimation of electronic properties. To avoid the expensive calculation of long-range HF exchange, this term is replaced by long-range PBEsol exchange; details are inferred in the earlier work [34].

In any event, this choice of parameters for HSE06-PBEsol is identical to the recent work of Schimka *et al.* [35], who have found that this works well for a range of solids, and also of McDonnell *et al.* [34], both with an exact-exchange contribution of 25%. However, in this study we 'tune' the exact-exchange contribution parameter 'α' in eqn. 1 of Ref. 25, 34 so as to result in better agreement of the lattice parameters and band gap with our experiment and earlier findings [35].

Bulk calculations were performed on symmetric slab (2 × 1 × 1) within a supercell comprising a total of 60 atoms. A 2 × 2 × 2 Gamma-centered *k*-point mesh [36] was applied over the Brillion zone and detailed computational methodology is incurred in Supplementary Information which is sufficient in precision for the calculation of ground-state geometry and optical properties.

In the present work, the frequency-dependent dielectric matrix has been determined after the electronic ground state for the optical properties of BFO. Inter-band contributions to the imaginary part $\varepsilon_2(\omega)$ of dielectric tensor $\varepsilon(\omega)$ were calculated by summation over empty states. The real part of the dielectric tensor $\varepsilon_1(\omega)$ was obtained by the usual Kramers-Kronig transformation [37]. For the optical functions, details are inferred in Supplementary Information.

## 3. Results and Discussion

The phase composition and structure of the as-prepared and post-leaching BFO powder were examined using XRD (cf. Fig. 1). All peaks were identified according to card number JCPDS 86-1518 indicating phase-pure BFO after leaching. In the as-prepared powder, as expected, impurity phases of $Bi_2Fe_4O_9$, $Bi_2O_3$ and $Bi_{25}FeO_{39}$ exist and are denoted in Fig. 1 with an asterisk [10]. Secondary unwanted peaks, associated with the substrate holder, are assigned with the letter *h*. The holder's spectrum is provided in Supplementary Information (cf. Fig. S1). Further analysis of XRD spectra studies show that the peaks near 39 and 57° are split; this is indicative of the rhombohedral distortion of BFO [8].

Particle-size and SEM analysis were undertaken on the powder. Figure 2 depicts the Sauter mean diameter (SMD) after leaching to be around 12 μm, with a particle size distribution of between 1 and 60 μm. The SEM analysis also shown in Fig. 2 (on the right) corroborates this result, showing the majority of the particles to be of the size range indicated by particle size analysis. The pure micron-sized BFO powder synthesised, can be effectively considered bulk material due to its size, and hence justifies the latter comparison between bulk-phase theory and experiment (*vide infra*).

An important property of BFO is photo-activity. To observe if the micron-sized powder produced in this study exhibited such photo-catalytic properties, a comparative photo-

degradation study was undertaken between micron sized BFO and $TiO_2$, using methyl orange. $TiO_2$, in particular, its anatase crystalline variant, due to its wide use in photocatalysis, was used as a comparative material in this study. No discernible degradation of the stock methyl orange solution was noticed over the 7-hour testing period. For $BiFeO_3$, a 28% decrease was observed over the same time period. This result is comparable with that seen in Ref. 8; there, as in the present study, the larger micron size powder was observed to be less photoactive than its nano-sized counterpart. Although this is mainly due to the amount of available surface area present to interact with the dye molecules, the smaller particles also stay in suspension easier; hence a greater extent of the dye is degraded more rapidly. The $TiO_2$ powder used showed a SMD particle size of around 1 μm, with a large proportion of particles below this size resulting in 100% degradation (cf. Fig. 3), over the same period.

Figure 4(a) shows the UV-vis absorption spectra for experimentally synthesised BFO with DFT results overlaid thereon, via a cubic spline interpolation and least-squares regression-fitting procedure. The experimental data is averaged over three independent measurements, with the standard deviations shown. There is a correlation coefficient of 89% between experimental and theoretical results within the energy range of ~1.6 to 3.2 eV. The main edge of absorption starts at around 2.1 eV and the leading-edge peak of the ~2.5 eV shoulder represents the onset of optical absorption; this is suggestive of excitonic character, and is due to metal-to-metal transitions. This peak is more prominent in the theoretical calculations because of the use of Gaussian smearing of 0.1 eV, and lies within the standard deviation of experimental calculations. The $Fe^{3+}$ ion has half-filled ($3d^5$) configurations, which is an octahedral as well as tetrahedral crystal field gives rise to a $^6A_{1g}$ ground state. Since this is the only sextet state, all crystal field transitions are both spin and octahedral symmetry partly forbidden. In tetrahedral symmetry, the later selection rule is slightly relaxed. Nevertheless these transitions are extremely weak. The position of this transition depends on crystal-field

strength. More the crystal field, transition shifts to lower energy. The band shoulder around 1.7 eV, can be assigned to a $Fe^{3+}$ crystal field excitation ($^6A_{1g} \rightarrow {}^4A_{1g}$) [38] which does not appear in the theoretical modelling used in this study. The DFT+U ('U'- Mott Hubbard correction) approach can tackle this issue as it works mainly for *d*-electron, which can be sufficient to take account of *d* to *d* crystal-field excitation. In contrast, this approach may break the spin and orbital symmetry of correlated metals or insulators. As a consequence, DFT+DMFT (Dynamical Mean Field Theory) method is implemented to come over this issue, specially for correlated system, but it is numerically high in cost [39]. However, this kind of absorption edge estimation is strongly dependent on sample morphology and quality [40].

Here, the band gaps for both theoretical and experimental measurements were calculated using the conventional Tauc method and taking the value of the extrapolation of the linear portion of the graph with the abscissa. The experimental direct and indirect band gaps thus inferred were 2.10 and 1.92 eV, respectively, comparable to the corresponding respective theoretical predictions of 2.14 and 1.83 eV, showing good, quantitative agreement between both sets (see Fig.4 (b) and (c)). These values obtained are not only comparable to each other but also for other studies of BFO observed in the literature, e.g., Ref. 9. The good level of agreement between state-of-the-art DFT and experiment tends to arise largely from the use of hybrid functionals in the guise of HSE06, but also the use of the PBEsol approach to improve the optimal geometry for the solid-state.

The calculated projected density of states, the band structure and calculated optical constants are shown in Figs. 5, 6 and 7 (a-g), respectively. We consider here only the spin-up case for Fe ion which has distinct features from spin-down state and the highest occupied state is set at 0 eV. As can be seen from Fig. 5, the peak due to the Bi 6*s* state is located at around –10 eV. In the valence band, the small proportion of O 2*p* states mix with Fe 3*d* and

Bi 6*p* states and spread over the range of 0 to – 6.6 eV. Above the Fermi level, the conduction band is mostly characterised by Fe 3*d* state dominating other states, with a small contribution from Bi 6*p* orbitals. Fig. 6 reveals that the BFO has an indirect band gap (with the gap between the top of valence band near to L and the bottom of conduction band is along L). The indirect and direct band gaps are around 1.9 and 2.1 eV, respectively, in good agreement with our experimental results, and those inferred from the 'Tauc' approach.

Fig. 7 (a-g) shows the calculated results real part of the optical conductivity $\sigma_1(\omega)$, index of refraction ($n$), extinction coefficient ($k$), energy-loss spectrum ( $L_s(\omega)$ – surface and $L(\omega)$ – bulk), reflection coefficient ($R$), and real part of inter-band transition strength ($Re\ J_{cv}$). The broad peaks in the bulk energy-loss spectrum are at about 11, 23 and 30 eV, relating to transitions from occupied O 2s, Bi 6s and O 2p bands lying below the valence band to the conduction band. In addition, the featured peaks at around 14, 20, and 29.5 eV in the real part of the inter-band transition strength (Re $J_{cv}$) are attributable to electronic transitions from occupied O 2*s* energy levels to lower in the empty conduction band of BFO. The index of refraction and extinction coefficients are directly proportional to the real and imaginary part of dielectric constant, respectively. The static refractive index (at $n = 0$) is 2.7, while the maximum occurs at 2.2 eV. The plasmon peak is found around at 30 eV.

## 4. Conclusions

Micron-sized, photo-catalytically active BFO was synthesised experimentally using a solid-state reaction. The powder was observed from XRD to be phase-pure and irregular in shape from SEM analysis. A drop in concentration of 28% for BFO in methyl orange was observed over a 7-hour period although less than the 100% degradation observed from the $TiO_2$ this can be attributed to smaller particulate size and the resultant better suspension of the powder in the solution. As remarked previously, various previous experimental studies do indeed produce a range of sometimes-contradictory result for the band gap, due primarily to

variations in particle size and morphology and the thin-film thickness. This is challenging for direct comparison of (bulk-state) DFT calculations for band-gap properties with thin-film experimental data, quite apart from the performance of the functional itself. Nonetheless, direct and indirect band gaps of 2.10 and 1.92 eV were inferred from UV-vis data, respectively, and these gaps are comparable to the corresponding respective hybrid-DFT predictions of 2.14 and 1.83 eV. A correlation of ~89% between experimental and theoretical results for the absorption coefficient was achieved, suggesting that hybrid-DFT may be approaching the point where it can predict more accurately optical constants for such multiferroelectric materials. It was also shown that the underlying band gap is indirect from examination of electronic band structure. These results show that even though the standard value viz. ¼ of exact-exchange in hybrid functionals seems to provide rather accurate band gap, clearly a smaller exact-exchange (10% in this work) is necessary to obtain better results.

**Acknowledgments**

This work was supported by the Science Foundation Ireland (SFI) Research Frontiers Programme (reference No. 10/RFP/MTR2868) and Precision Strategic Research Cluster Grant No.08/SRC/I1411. The authors thank Run Long, Sankha Ghosh and J.M.D. MacElroy for useful discussions, and Science Foundation Ireland (SFI) and the Irish Centre for High End Computing for the provision of computational resources, in addition to productive interactions with the SFI-funded Strategic Research Cluster on Advanced Biomimetic Materials for Solar Energy Transformation (reference No. 07/SRC/B1160).

## References


[1] J.M. Moreau, C. Michel, R. Gerson, W.J. James, Journal of Physics and Chemistry of Solids 32/6 (1971) 1315.
[2] G.A. Smolenskiĭ, I.E. Chupis, Soviet Physics Uspekhi 25/7 (1982) 475.
[3] F. Gao, X. Chen, K. Yin, S. Dong, Z. Ren, F. Yuan, T. Yu, Z. Zou, J.M. Liu, Advanced Materials 19/19 (2007) 2889.
[4] J.-H. Xu, H. Ke, D.-C. Jia, W. Wang, Y. Zhou, Journal of Alloys and Compounds 472/1–2 (2009) 473.
[5] S. Shetty, V.R. Palkar, R. Pinto, Pramana 58/5 (2002) 1027.
[6] Y.P. Wang, L. Zhou, M.F. Zhang, X.Y. Chen, J.M. Liu, Z.G. Liu, Applied Physics Letters 84/10 (2004) 1731.
[7] D. Maurya, H. Thota, K.S. Nalwa, A. Garg, Journal of Alloys and Compounds 477/1–2 (2009) 780.
[8] S. Li, Y.-H. Lin, B.-P. Zhang, C.-W. Nan, Y. Wang, Journal of Applied Physics 105/5 (2009) 056105.
[9] S.K. Srivastav, N. S. Gajbhiye, Journal of the American Ceramic Society 95/11 (2012) 3678.
[10] M.M. Kumar, V.R. Palkar, K. Srinivas, S.V. Suryanarayana, Applied Physics Letters 76/19 (2000) 2764.
[11] D.I. Bilc, R. Orlando, R. Shaltaf, G.M. Rignanese, J. Íñiguez, P. Ghosez, Physical Review B 77/16 (2008) 165107.
[12] S.J. Clark, J. Robertson, Applied Physics Letters 94/2 (2009) 022902.
[13] J.B. Neaton, C. Ederer, U.V. Waghmare, N.A. Spaldin, K.M. Rabe, Physical Review B 71/1 (2005) 014113.
[14] A. Stroppa, S. Picozzi, Physical Chemistry Chemical Physics 12/20 (2010) 5405.
[15] S.R. Basu, L.W. Martin, Y.H. Chu, M. Gajek, R. Ramesh, R.C. Rai, X. Xu, J.L. Musfeldt, Applied Physics Letters 92/9 (2008) 091905.
[16] F. Gao, Y. Yuan, K.F. Wang, X.Y. Chen, F. Chen, J.M. Liu, Z.F. Ren, Applied Physics Letters 89/10 (2006) 102506.
[17] A.G. Gavriliuk, V.V. Struzhkin, I.S. Lyubutin, S.G. Ovchinnikov, M.Y. Hu, P. Chow, Physical Review B 77/15 (2008) 155112.
[18] U.A. Joshi, J.S. Jang, P.H. Borse, J.S. Lee, Applied Physics Letters 92/24 (2008) 242106.
[19] T. Kanai, S.-i. Ohkoshi, K. Hashimoto, Journal of Physics and Chemistry of Solids 64/3 (2003) 391.
[20] A. Kumar, R.C. Rai, N.J. Podraza, S. Denev, M. Ramirez, Y.-H. Chu, L.W. Martin, J. Ihlefeld, T. Heeg, J. Schubert, D.G. Schlom, J. Orenstein, R. Ramesh, R.W. Collins, J.L. Musfeldt, V. Gopalan, Applied Physics Letters 92/12 (2008) 121915.
[21] R. Palai, R.S. Katiyar, H. Schmid, P. Tissot, S.J. Clark, J. Robertson, S.A.T. Redfern, G. Catalan, J.F. Scott, Physical Review B 77/1 (2008) 014110.
[22] D. A. Mich, Journal of Physical Chemistry C 113/9 (2009) 3530
[23] M. Goffinet, P. Hermet, D.I. Bilc, P. Ghosez, Physical Review B 79/1 (2009) 014403.
[24] Z.D. Pozun, G. Henkelman, The Journal of Chemical Physics 134/22 (2011) 224706.
[25] N. Wadnerkar, N. J. Engish, Computational Material Science (in press)
[26] M.N. Rashed, International Journal of Physical Sciences Vol. 2/3 (2007) 073.
[27] J. Heyd, G.E. Scuseria, M. Ernzerhof, The Journal of Chemical Physics 118/18 (2003) 8207.
[28] J. Heyd, G.E. Scuseria, M. Ernzerhof, The Journal of Chemical Physics 124/21 (2006) 219906.
[29] J. Paier, M. Marsman, K. Hummer, G. Kresse, I.C. Gerber, J.G. Angyan, The Journal of Chemical Physics 125/24 (2006) 249901.
[30] G. Kresse, J. Furthmüller, Physical Review B 54/16 (1996) 11169.
[31] G. Kresse, J. Hafner, Physical Review B 47/1 (1993) 558.
[32] J.P. Perdew, K. Burke, M. Ernzerhof, Physical Review Letters 77/18 (1996) 3865.
[33] J.P. Perdew, A. Ruzsinszky, G.I. Csonka, O.A. Vydrov, G.E. Scuseria, L.A. Constantin, X. Zhou, K. Burke, Physical Review Letters 100/13 (2008) 136406.

[34] K.A. McDonnell, N.J. English, M. Rahman, D.P. Dowling, Physical Review B 86/11 (2012) 115306.
[35] L. Schimka, J. Harl, G. Kresse, The Journal of Chemical Physics 134/2 (2011) 024116.
[36] H.J. Monkhorst, J.D. Pack, Physical Review B 13/12 (1976) 5188.
[37] M. Gajdoš, K. Hummer, G. Kresse, J. Furthmüller, F. Bechstedt, Physical Review B 73/4 (2006) 045112.
[38] S.T. Zhang, M.H. Lu, D. Wu, Y.F. Chen, N.B. Ming, Applied Physics Letters 87/26 (2005) 262907.
[39] B. Amadon, Journal of Physics: Condensed Matter 24 (2012) 075604.
[40] (a) G. Zhou,M. Lu, F. Gu, S. Wang, Z. Xiu, X. Chang, Journal of Crystal Growth 270 (2004) 280. (b) B. B. Kale, J. O Baeg, S. M. Lee, H.Chang, S. J. Moon, C.W. Lee Advanced Functional Material 16 (2006) 1349 (c) A. P. Alivisatos, Science 271 (1996) 933.

**Figure Captions:**

**Fig. 1.** X-ray diffraction spectra for BFO, pre- and post-leaching. Spectra for the substrate holder peaks indicated by "h" can be found in Supplementary Information Figure S1.

**Fig. 2.** Particle size analysis (left) and SEM image (right) at 250 x of the BFO powder after leaching.

**Fig. 3.** Photo-catalytic degradation study absorption spectra (a) Methyl Orange, (b) BFO, (c) $TiO_2$, (d) Comparison of degradation rates for each material.

**Fig. 4.** (a) Absorption spectra comparing theoretical and experimental results. Shown in the inset is an enlargement of the absorption spectra with wavelength in nm, indicating the variation in results. Comparisons between (b) direct and (c) indirect optical band gaps with experimental and theoretical results.

**Fig. 5.** (Colour online) Ion-projected electronic densities of states for BFO using HSE06-PBEsol (with 10% exact exchange). The highest occupied state is set to 0 eV (dashed vertical line).

**Fig. 6.** Electronic band structure along high-symmetry k-points (Γ-L-F-T- Γ). The highest occupied state is set to 0 eV.

**Fig. 7.** Calculated optical functions for BFO: (a) the real part of optical conductivity $\sigma_1(\omega)$ (in $10^3\ \Omega^1 cm^{-1}$), (b) the bulk energy-loss function, $L(\omega)$, (c) the surface energy-loss function, $L_s(\omega)$, and (d) extinction coefficient, *k* (e) reflection coefficient, R (f) index of refraction, *n* (g) the real part of the inter-band transition strength, Re $J_{cv}(\omega)$

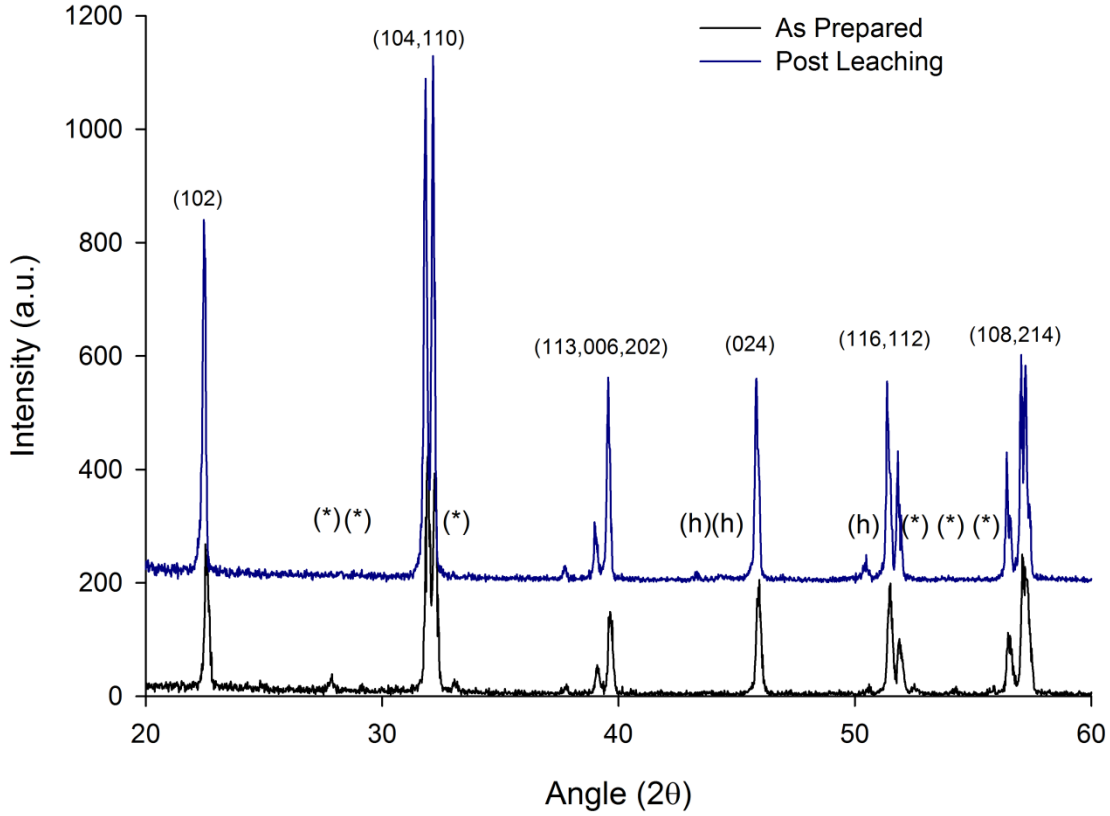
As Prepared
Post Leaching
(104,110)
(102)
(113,006,202)
(024)
(116,112)
(108,214)
(*)(*)
(*)
(h)(h)
(h)
(*)
(*)
(*)
Intensity (a.u.)
Angle (2θ)
0
200
400
600
800
1000
1200
20
30
40
50
60

**Fig. 1.**

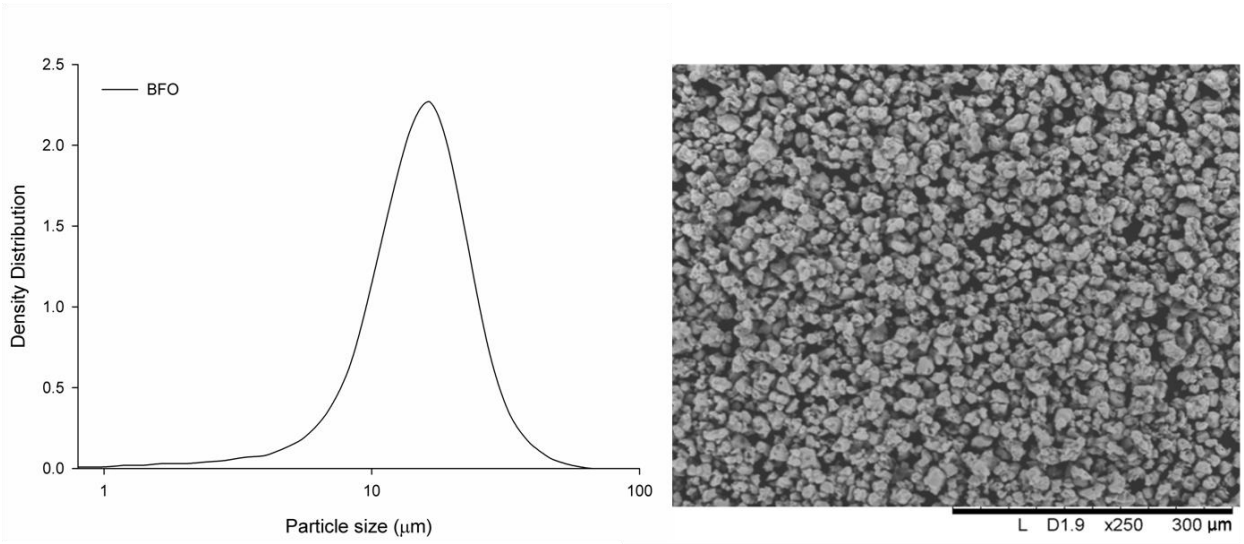
BFO
Density Distribution
2.5
2.0
1.5
1.0
0.5
0.0
1
10
100
Particle size (μm)
L D1.9 x250 300 μm

**Fig. 2.**

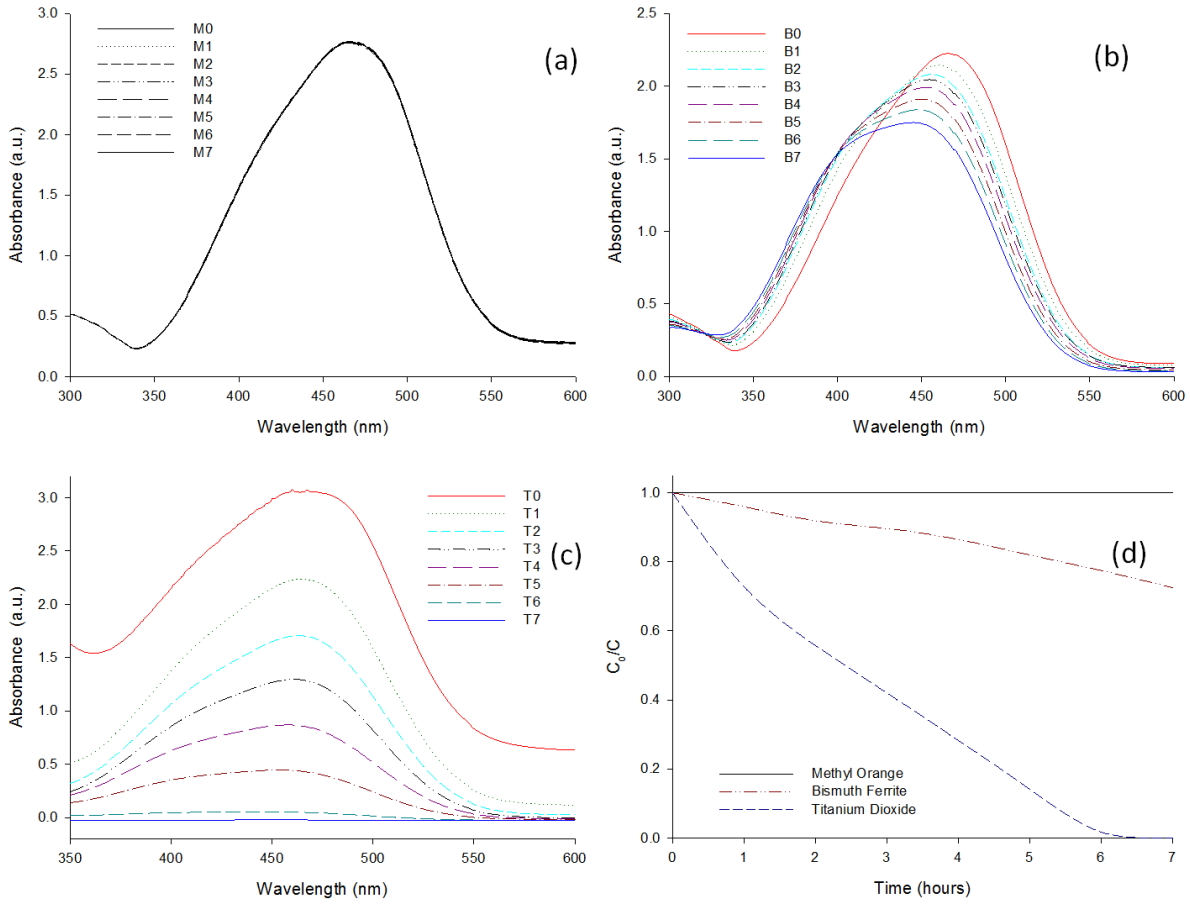
(a)
M0
M1
M2
M3
M4
M5
M6
M7
Absorbance (a.u.)
Wavelength (nm)
(b)
B0
B1
B2
B3
B4
B5
B6
B7
Absorbance (a.u.)
Wavelength (nm)
(c)
T0
T1
T2
T3
T4
T5
T6
T7
Absorbance (a.u.)
Wavelength (nm)
(d)
Methyl Orange
Bismuth Ferrite
Titanium Dioxide
C0/C
Time (hours)

**Fig. 3.**

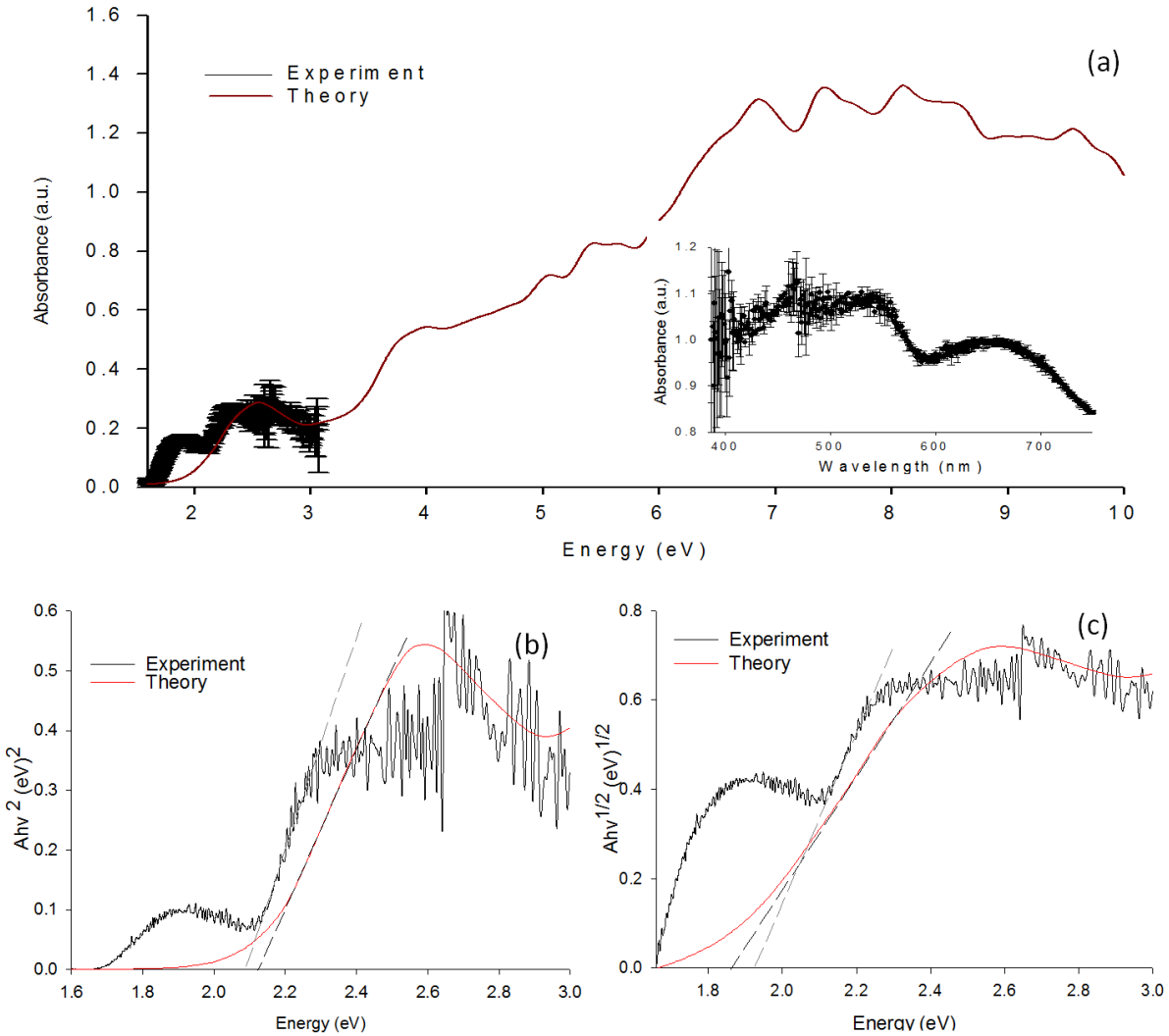
(a)
Experiment
Theory
Absorbance (a.u.)
Energy (eV)
Wavelength (nm)
(b)
Experiment
Theory
Ahv 2 (eV)2
Energy (eV)
(c)
Experiment
Theory
Ahv 1/2 (eV)1/2
Energy (eV)

**Fig. 4.**

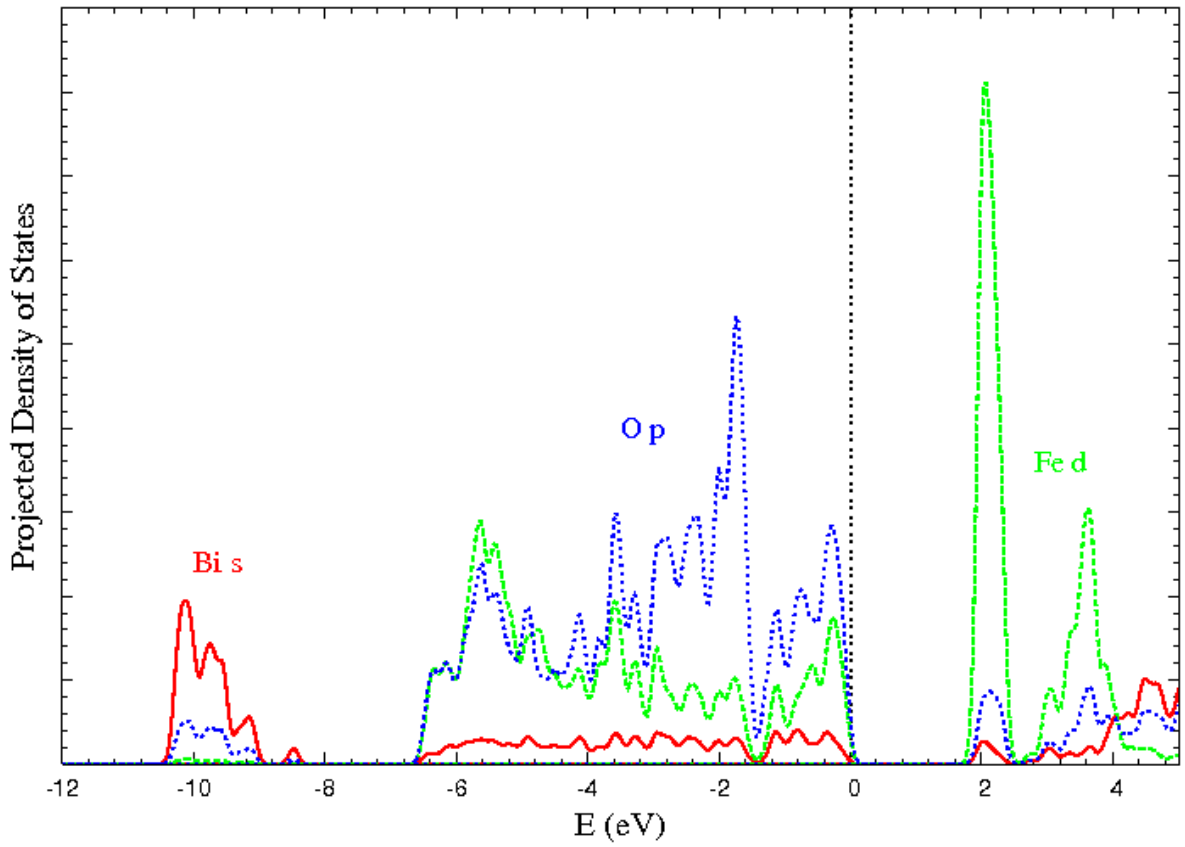


**Fig. 5**

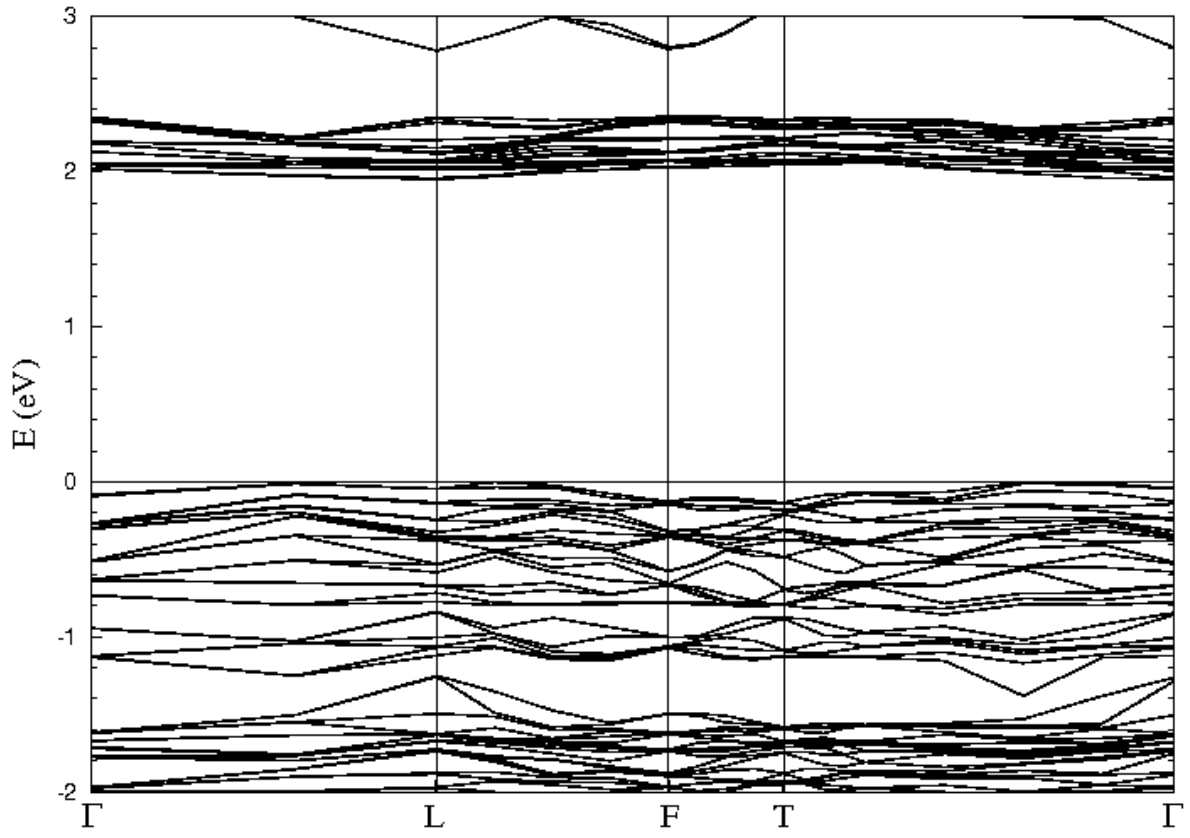


**Fig. 6**

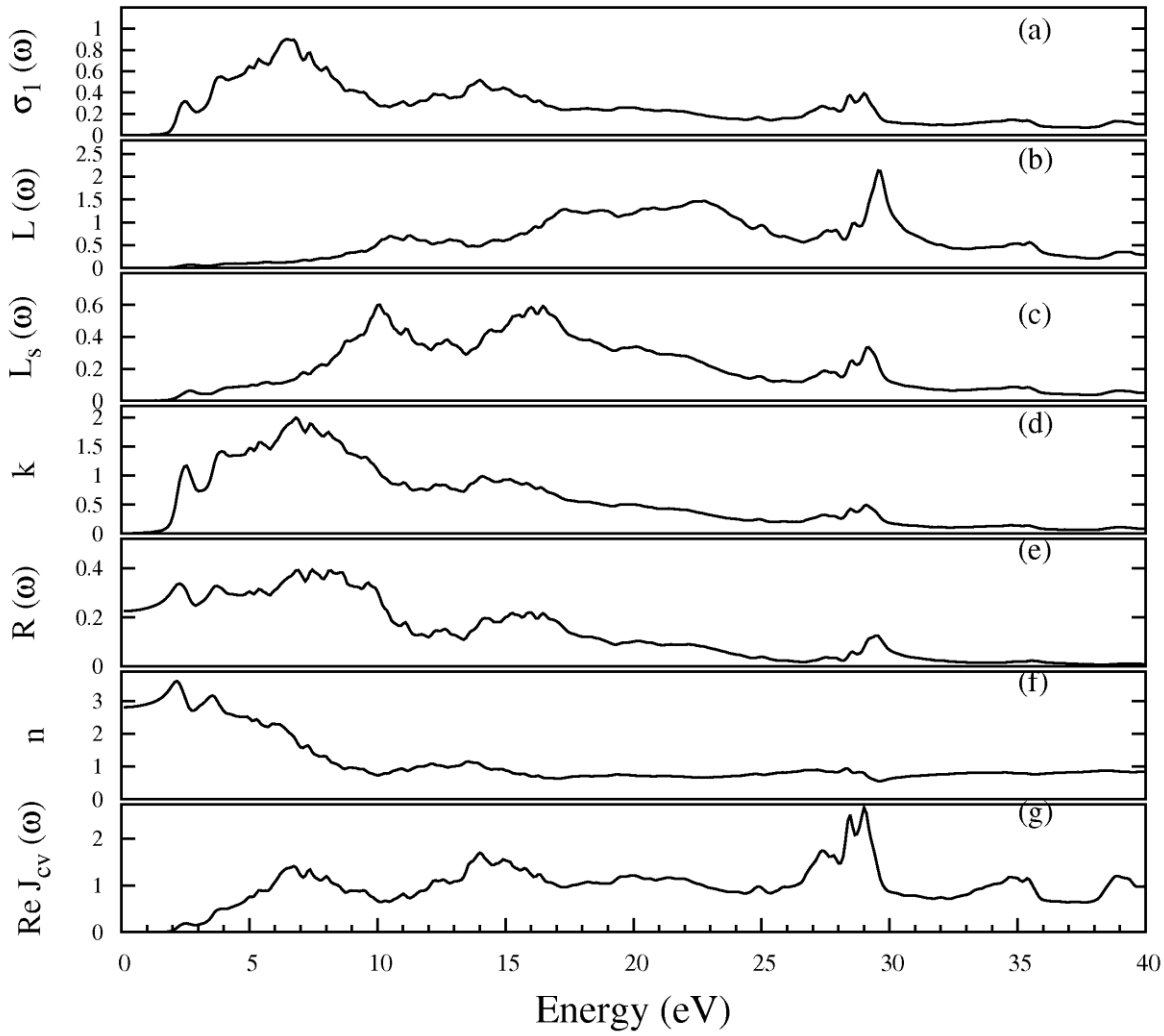


**Fig. 7**